Lipid Sponge Droplets as Programmable Synthetic Organelles

Ahanjit Bhattacharya[1,†], Henrike Niederholtmeyer[1,†], Kira A. Podolsky[1], Rupak Bhattacharya[2], Jing-Jin Song[2], Roberto J. Brea[1], Chu-Hsien Tsai[1], Sunil K. Sinha[2], and Neal K. Devaraj[1, *]

[1]Department of Chemistry and Biochemistry, University of California, San Diego, 9500 Gilman Drive, Natural Sciences Building 3328, California 92093, United States.

[2]Department of Physics, University of California, San Diego, 9500 Gilman Drive, Mayer Hall Addition 4561, California 92093, United States.

*Correspondence to: ndevaraj@ucsd.edu

[†]These authors contributed to this work equally

Abstract

Living cells segregate molecules and reactions in various subcellular compartments and locations. Spatial organization is likely essential for expanding the biochemical functions of synthetic reaction systems, including artificial cells. Here we describe programmable synthetic organelles based on highly stable lipid sponge phase droplets that spontaneously assemble from a galactose-derived single-chain lipid and non-ionic detergents. Fluorescent dyes and biologically relevant molecules partition into droplets based on their size, polarity, and specific binding motifs. The sequestration of macromolecules can be further programmed by the addition of suitably functionalized amphiphiles to the droplets. We demonstrate that droplets can harbor functional soluble and transmembrane proteins, allowing for the co-localization and concentration of enzymes and substrates to enhance reaction rates. Droplets protect bound proteins from proteases, and these interactions can be engineered to be reversible and optically controlled. Lipid sponge droplets permit the facile introduction of membrane environments and self-assembling spatial organization into biochemical reaction systems.

1

Introduction

Compartmentalization is a defining feature of life. Eukaryotic cells are characterized by their membrane-bound and membraneless organelles[1] and in prokaryotic cells, different processes are precisely organized in subcellular locations and microcompartments[2]. Spatial organization allows cells to co-localize and concentrate molecules, establish concentration gradients, separate incompatible reactions, and regulate reactions by controlling the availability of reactants. The biochemical capabilities of "bottom up" cell-mimics and synthetic reaction systems built to date lag behind those of living cells, in part due to a lack of programmable compartmentalization capabilities.

Several methodologies have been developed to sequester specific biochemical processes to defined locations and to emulate functions of natural cellular organelles[3]. In eukaryotic cells, compartmentalization is primarily achieved by lipid bilayer membranes that demarcate the boundary to the outside world and enclose classical organelles. Membrane-bound vesicles have been extensively utilized as experimental model systems to emulate some of the fundamental features of a cell[4] as well as that of organelles like chloroplasts[5,6] and nuclei[7]. Nested vesicle-in-vesicle assemblies have also been utilized to separate molecules until a trigger event[8]. Alternatively, coacervates, which form by liquid-liquid phase separation and are typically composed of oppositely charged polyions or immiscible polymers[9], mimic the liquid and dynamically assembling membraneless organelles found in eukaryotes such as the nucleoli, stress granules, and P-bodies[1]. Coacervates are molecularly crowded systems and open to the surrounding environment. Their ability to spontaneously enrich molecules from the environment has led to enhanced reaction rates for ribozymes[10], improved transcription[11], and acceleration of enzymatic reactions[12]. Coacervates have also been engineered to reversibly assemble and disassemble to control the release of sequestered molecules in response to enzyme activity[13] or temperature[14], and to be surrounded by fatty acid membranes to modify their permeability[15]. DNA-loaded hydrogels in gene expression reactions have confined transcription to compartments that loosely emulate the eukaryotic nucleus[16–18]. Other synthetic compartmentalization strategies localize and separate reactions in artificial containers based on proteins[19,20], synthetic polymers[21], and Pickering emulsions[22].

Artificial organelles should ideally self-assemble and be programmable to sequester a wide range of molecules and reactions with high efficiency and selectivity. They should also allow for dynamic and reversible changes in sequestration behavior to allow precise spatiotemporal regulation. While coacervates may fulfill these requirements, they fail to capture a crucial property of many natural cellular organelles such as the endoplasmic reticulum (ER), Golgi apparatus, mitochondria and chloroplasts. These organelles are not only enclosed by membranes but contain extremely high densities of tightly packed membrane networks. In eukaryotic cells, the ER is often the organelle with the greatest surface area and may contain 50-60% of the total membrane[23]. Lipid membranes of the ER form a vast convoluted network interspersed by aqueous channels. Due to the presence of numerous hydrophobic and hydrophilic volumes, the ER hosts a diversity of soluble and membrane-bound proteins to carry out biochemical transformations. Nuances of such highly membranous organelles cannot be captured by vesicle-derived artificial organelle models nor by complex coacervates.

Bicontinuous lipidic materials such as sponge phases (also referred to as L_3 phase, molten cubic phase, or lipid coacervates) possess properties that resemble highly membranous organelles such as the ER. They contain a highly convoluted and interconnected three dimensional network

2

of lipid bilayers intersected by similarly interconnected nanometer sized aqueous channels[24,25]. Bicontinuous lipid phases (sponge and cubic) offer enormous membrane surface areas, the capacity to harbor both hydrophobic and hydrophilic molecules, and the ability to sequester soluble and membrane proteins[26]. Sponge phases have been observed in dispersions of non-ionic surfactants[27], alkylammonium salts[28], Aerosol OT[25], gemini surfactants[29], glycolipid biosurfactants[30], and monoglycerides[31]. Sponge phases frequently form a single bulk phase, exist only within a narrow range of concentration, pH, and temperature, and are highly sensitive to additives.

Recently, we reported the discovery of a series of lamellar membrane-forming single-chain amphiphiles derived from galactopyranose and unsaturated fatty acids[32,33]. During our studies, we discovered that N-oleoyl β-D-galactopyranosylamine (GOA, **Fig. 1a**) forms micron-sized spherical droplets in aqueous media in presence of the commercially available non-ionic octylphenoxypolyethoxyethanol surfactant IGEPAL® CA-630 (IGEPAL, **Fig. 1a**). Using a combination of physical and biochemical techniques we found that the droplets consist of a lipid sponge phase that is stable and compatible with a wide range of biological reaction systems. We demonstrate that uptake of specific biomolecules such as nucleic acids and proteins into the droplets can be predictably programmed by doping sponge phase droplets with small quantities of amphiphiles bearing affinity groups. Moreover, the lipid bilayer-rich nature of the droplets allows spontaneous reconstitution of functional transmembrane proteins to emulate the biosynthetic functions of the endomembrane system. To mimic additional organelle functions, we demonstrate that co-localization and concentration of an enzyme and its substrate in droplets enhanced the rate of a biochemical reaction, and that reversible light-controlled sequestration and release of a protein can be used to regulate an enzymatic reaction. Lipid sponge droplets thus offer a unique platform for mimicking both membrane- and solution-associated organelle functions.

Results and discussion

Formation and physical characterization of lipid sponge droplets. We synthesized N-oleoyl β-D-galactopyranosylamine (GOA, **Fig. 1a**) as previously described[33]. When a thin lipid film of GOA deposited on the walls of a glass vial is hydrated with a solution containing the non-ionic detergent IGEPAL (**Fig. 1a**), a uniformly turbid dispersion is produced. On centrifugation or long standing, the dispersion coalesces into an optically isotropic single dense phase at the bottom of the tube (**Fig. 1b**). By phase contrast microscopy, the dispersion was found to consist of a polydisperse population of micron-sized spherical droplets with distinct optical contrast compared to the surrounding medium (**Fig. 1c**). The spherical shape suggested to us that the droplets are liquid in nature. The coalesced phase can be resuspended by gentle agitation or vortexing. We used high-performance liquid chromatography and mass spectrometry (HPLC-MS) to determine the compositions of the supernatant and the coalesced phases and found that both amphiphiles had partitioned almost entirely (~99%) into the coalesced phase (**Supplementary Fig. 1**). When thermogravimetric analysis (TGA) was carried out on the coalesced phase (obtained from 4:3 GOA:IGEPAL by molar ratio), we observed a gradual loss of about 67% mass over the range 30-100 °C (**Supplementary Fig. 2**). This lost mass is likely originating from water present in the coalesced phase. We acquired the fluorescence emission spectrum of the solvatochromic dye Laurdan incorporated in the droplets and obtained a maximum around 490 nm (**Supplementary Fig. 3**). This data suggests that the droplets have a water-accessible environment where the dye can undergo dipolar relaxation typical of fluid lipid membranes. In comparison, in oil-in-water droplet systems such as oleic acid, Laurdan exhibits a maximum peak at 440 nm. We constructed

3

a phase diagram by varying the relative proportions of GOA and IGEPAL and found that droplet formation takes place at molar ratios of approximately 1:1 to 1:4 (IGEPAL:GOA) occupying a large portion of the phase space (**Fig. 1d**). Outside this region, micellar solutions (at higher relative IGEPAL concentrations) or lamellar vesicles (at lower relative IGEPAL concentrations) are obtained.
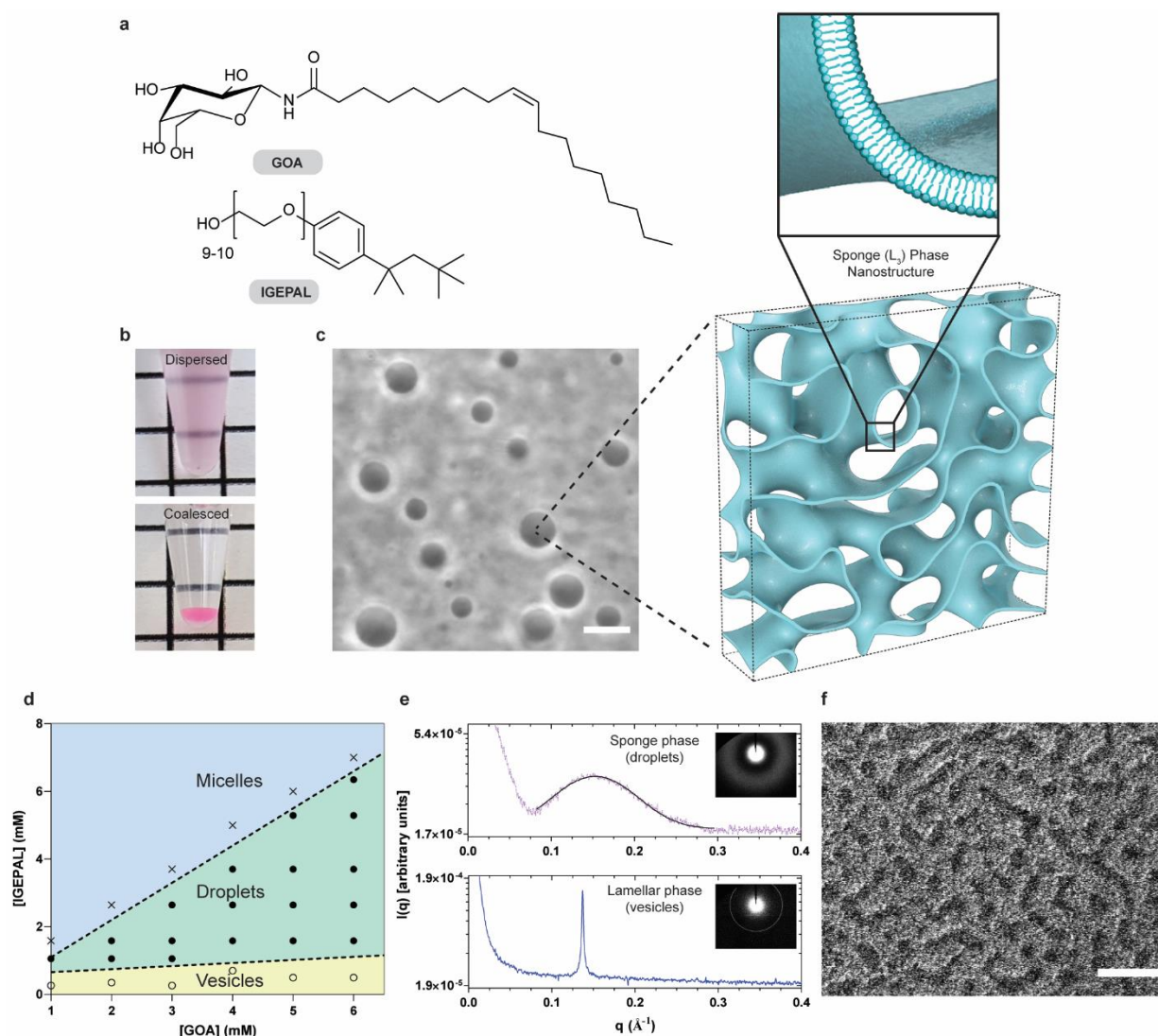

Fig. 1 | Physical characterization of the lipid sponge droplets. **a**. Chemical structures of *N*-oleoyl β-galactopyranosylamine (GOA) and octylphenoxypolyethoxyethanol (IGEPAL). **b**. A dispersed sample of droplets merges into a single coalesced phase at the bottom of the tube under gravity. A small quantity of water soluble dye Rhodamine B was added to the dispersion to demarcate the coalesced phase. **c**. Phase-contrast image of a typical droplet dispersion and illustration of the droplets' porous, bilayer-rich nanostructure. Illustration was based on a computationally generated model of a bicontinuous structure[54]. Scale bar: 10 μm. **d**. Phase diagram showing the relative molar compositions of GOA and IGEPAL in 1X PBS over which vesicles (*yellow*), droplets (*green*), and micelles (*blue*) are obtained. **e**. Top: synchotron small-angle X-ray scattering (SAXS) intensity profile (dotted) from a droplet dispersion (4:3 GOA:IGEPAL by molar ratio). The solid black line represents a Gaussian fit to the data to obtain the position of maximum. Bottom: synchotron SAXS intensity profile from a dispersion of GOA vesicles. The inset images show the diffraction patterns. **f**. Freeze-fracture cryogenic scanning electron microscopy (cryo-SEM) image corresponding to sponge phase morphology. Scale bar: 1 μm.

4

We carried out small-angle X-ray scattering (SAXS) investigation on droplet dispersions using a synchrotron radiation source. When the intensity [$I(q)$] profile from a 4:3 GOA:IGEPAL droplet dispersion was plotted against the scattering vector (q), a single broad peak was obtained (**Fig. 1e**). The peak is fitted to a Gaussian distribution and a maximum is obtained at q_{max} = 0.153±0.0002 Å^{-1}. For various compositions of the droplets, the intensity profile showed a decay behavior as $I(q) \approx q^{-2}$ consistent with a local bilayer structure (**Supplementary Fig. 4**)[34]. Such features are typical of a lipidic sponge (L$_3$) phase (**Fig. 1c**) similar to that reported with various surfactant systems[31,34]. The characteristic length (d = $2\pi/q_{max}$) for the sponge phase (from 4:3 GOA:IGEPAL) was calculated to be 4.11 nm. This length can be interpreted as the average channel diameter of the sponge phase[31]. We found that the nature of the peak and the position of the maxima of the SAXS profile remains nearly unchanged in the coalesced phase, suggesting that the structural characteristics are retained (**Supplementary Fig. 5**). In comparison, SAXS on a dispersion of GOA vesicles gave rise to an intensity profile consisting of a sharp peak (**Fig. 1e**) consistent with a lamellar (L$_\alpha$) phase[35].

We further characterized the droplets by cryogenic transmission electron microscopy (Cryo-TEM) and found that they lack any well-ordered internal structure, consistent with the characteristics of a sponge phase (**Supplementary Fig. 6a**)[36]. In contrast, Cryo-TEM analysis of a sample of GOA vesicles showed distinct membrane bound structures of various lamellarities (**Supplementary Fig. 6b**). We imaged the droplets by freeze-fracture cryogenic scanning electron microscopy (Cryo-SEM) and observed a porous morphology (**Fig. 1f**) corresponding to a three-dimensional network of lipid bilayers[25,28,30]. In addition to IGEPAL, we found that GOA forms droplets with other nonionic octylphenoxypolyethoxyethanol detergents such as Triton X-114 and Triton X-100 (**Supplementary Fig. 7**). Single chain galactolipids with shorter unsaturated fatty acid chains[33] such as GPOA and GMOA were also found to form droplets with the same class of non-ionic surfactants (**Supplementary Fig. 7**). Previously, it has been proposed that transformations of lamellar to sponge phases are mediated by bending of bilayers followed by formation of interconnections between them[24]. GOA and similar galactolipids alone form lamellar phases, which are composed of locally flat stiff bilayer membranes. We speculate that octylphenoxypolyethoxyethanol surfactants, with their flat aromatic ring and short aliphatic segment, insert between the GOA molecules and induce a negative curvature. Additionally, the detergents may make the bilayers more fluid by lowering the bending rigidity. These combined effects would allow adjacent bilayers to fuse and form a three-dimensional sponge-like network.

We found that stable droplets can be formed over a wide range of pH, ionic strength, buffer composition, and dilution. We observed droplet formation over the pH range 2-10, high ionic strength (up to 1 M NaCl), high concentrations of Mg^{2+} (100 mM) and Ca^{2+} (10 mM) (**Supplementary Fig. 8a-b**). The droplets also formed in complex media like sea water, cell culture media, and cell-free transcription/translation (TX-TL) reactions (**Supplementary Fig. 8c-e**). Due to lack of an ionizable head group, glycolipid sponge droplets assemble more robustly compared to other droplet systems based on single chain amphiphiles, such as fatty acids[37], which can exist only within a relatively narrow range of pH conditions and ionic environments.
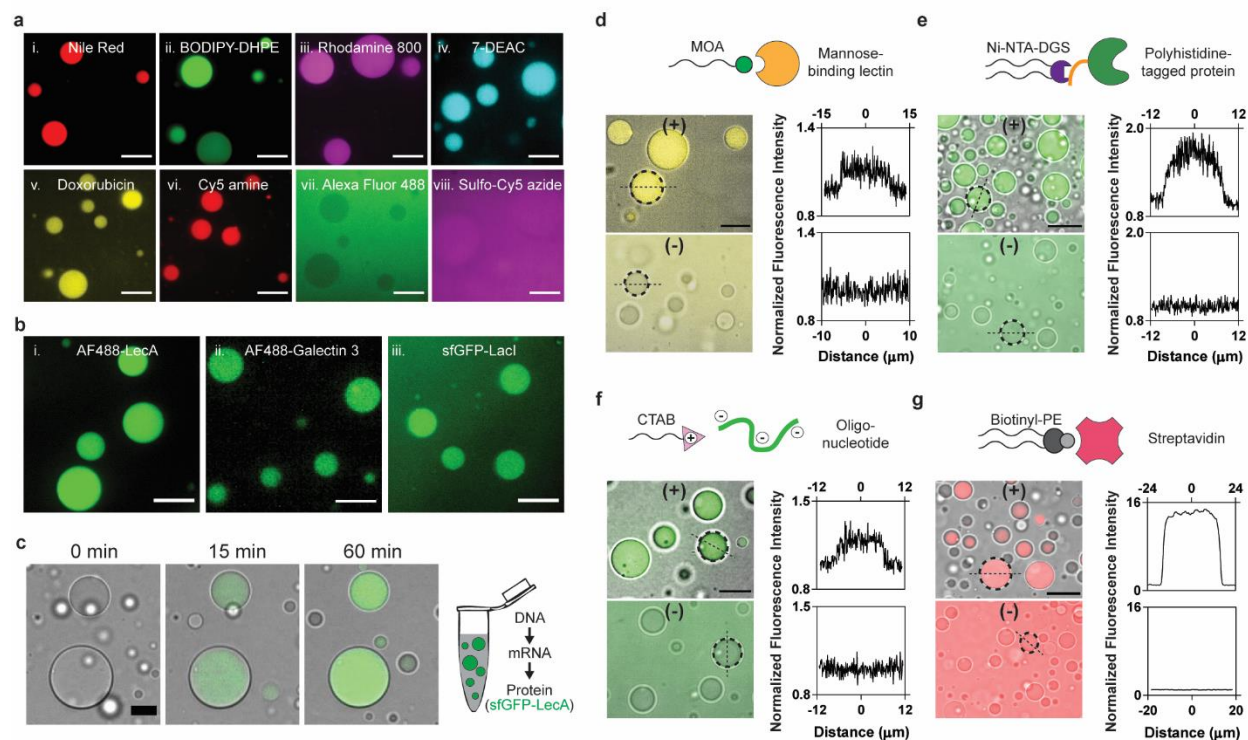
Fig. 2 | Partitioning of various molecules into lipid sponge droplets. **a**. Partitioning of i) Nile Red ii) BODIPY-DHPE iii) Rhodamine 800 iv) 7-diethylaminocoumarin v) Doxorubicin vi) Cy5-amine vii) Alexa Fluor 488 and viii) sulfo-Cy5-azide into lipid sponge droplets. Scale bars: 10 µm. **b**. Partitioning of galactophilic proteins i) Alexa Fluor 488-LecA ii) Alexa Fluor 488-Galectin 3 and iii) sfGFP-LacI into lipid sponge droplets. Scale bars: 10 µm. **c**. Time lapse images showing gradual incorporation of sfGFP-LecA expressed in PURE system into lipid sponge droplets. Scale bar: 15 µm. **d**. Selective partitioning of FITC-Concanavalin A into droplets doped with *N*-oleoyl β-D-mannosylamine (MOA). Scale bar: 15 µm. **e**. Selective partitioning of sfGFP-His$_6$ into droplets doped with Ni-NTA-DGS. Scale bar: 20 µm. **f**. Selective partitioning of a FAM-labeled DNA oligonucleotide into droplets doped with CTAB. Scale bar: 15 µm. **g**. Selective partitioning of Alexa Fluor 568-labeled streptavidin into droplets doped with biotinyl-PE. Scale bar: 35 µm. In **d-g**, binding (doped) droplets are represented by (+) while non-binding droplets are represented by (-). Plots of the fluorescence intensity profile along a straight line drawn through the center of the marked droplets (broken circle) are shown on the right. On the *x*-axes, 0 corresponds to the center of the droplets.

Partitioning of small molecules and fluorescent dyes. By virtue of their extensive bilayer network and high water content, lipid sponge droplets can provide a unique milieu for harboring molecules spanning from hydrophobic to hydrophilic in nature. At first, we studied the partitioning behavior of a variety of molecules into the sponge phase using HPLC-MS. We measured the concentration of an analyte in the supernatant and compared it with the total concentration to estimate the percentage of partitioning into the sponge phase (**Supplementary Table 1**). Polar lipid molecules such as cholesterol and 1-palmitoyl-2-oleoyl-glycero-3-phosphocholine (POPC) were 100% partitioned. Water soluble fluorescent dye Rhodamine B was 81.4% partitioned while the more polar dye Sulforhodamine B was 47.3% partitioned. Next we used fluorescence microscopy to visualize the partitioning behavior of several lipophilic, and water soluble fluorescent molecules (**Fig. 2a, Supplementary Fig. 9a**). Highly sulfonated dyes such as Alexa Fluor 488, and sulfo-Cy5-azide showed little or no enrichment (**Fig. 2a, vii-viii**). This suggests that dyes like Alexa Fluor 488 can be used as a fluorescent label for macromolecules to study their localization into the droplets in an unambiguous manner. Non-sulfonated xanthene dyes

such as fluorescein and 4′,5′-dibromofluorescein showed different degrees of partitioning depending on pH and hence their ionization state (**Supplementary Fig. 9b-c**). For instance, at lower pH (~6.0) the phenolic -OH of fluorescein remains mostly protonated, resulting in greater partitioning (43.7%) to the sponge phase. At higher pH (~8.0), the phenolic -OH is ionized, leading to significantly less partitioning (13.2%) to the sponge phase. Based on the above studies, we conclude that overall charge, hydrophobicity/hydrophilicity, and structure of the molecules play an important role in determining the partitioning behavior.

Partitioning of galactophilic proteins. Galactose and its derivatives play a crucial role in biology as affinity or recognition groups for protein binding on the surfaces of cells or organelles. GOA offers ample β-galactopyranosyl moieties throughout the bulk of the sponge droplets. We hypothesized that proteins with affinity for galactose residues would spontaneously partition into the droplets. We chose to test the well-studied galactophilic lectin LecA (PA-IL) from the pathogenic bacterium *Pseudomonas aeruginosa*, where LecA promotes biofilm formation via cross-linking between bacterial cell-surface galactose residues[38]. We added Alexa Fluor 488-labeled LecA (1 μM final concentration) to droplets (formed from 3 mM GOA and 1.8 mM IGEPAL) and observed a high extent of partitioning into the droplets (**Fig. 2b-i**). Using fluorometric analysis of the supernatant, we estimated that 97.3% of the protein partitioned into the droplets. We carried out control experiments where isopropyl β-D-1-thiogalactopyranoside (IPTG) or phenyl β-D-galactopyranoside were added as competing ligands for LecA and significantly less partitioning of the Alexa Fluor 488-labeled LecA was observed by microscopy, thus supporting our hypothesis that sequestration was due to a specific interaction of the lectin with GOA (**Supplementary Fig. 10**). Next we tested the galactophilic lectin galectin 3, which is known to bind primarily to β-galactoside residues and plays an important role in cell adhesion, macrophage activation, and apoptosis[39]. As expected, we observed highly efficient partitioning of Alexa Fluor 488-labeled galectin-3 into the droplets (**Fig. 2b-ii**). Apart from galactophilic lectins, we found that a GFP fusion of the *Escherichia coli lac* operon repressor protein (sfGFP-LacI) spontaneously partitions into the droplets (**Fig. 2b-iii**). LacI is known to bind to galactopyranoside effector ligands primarily via hydroxyl groups (O2, O3, O4, O6) of the galactose moiety on the latter. In addition, apolar substituents (if any) on the C1 (anomeric) position of galactose group interact with a hydrophobic surface in the binding site, thereby increasing the binding affinity[40]. We reason that the presence of the galactose group and hydrophobic oleoyl chain on GOA contribute to its binding to sfGFP-LacI.

Cell-free protein synthesis in the presence of droplets. To evaluate the compatibility of droplets and their sequestration properties with complex biochemical reactions, we formed droplets in a recombinant TX-TL system (PURExpress). The PURE TX-TL system consists of almost 30 enzymes, 56 tRNAs, ribosomes, and a highly optimized mixture of precursors and buffer components[41]. Even when droplets were present at high densities (reaction contained 12 mM GOA and 6.7 mM IGEPAL), efficient protein synthesis took place and we observed gradual sequestration of galactophilic proteins during their synthesis (**Fig. 2c, Supplementary Fig. 11, Supplementary Video 1**). While LecA and LacI fused with sfGFP spontaneously partitioned into the droplets upon synthesis, sfGFP alone did not (**Fig. 2c, Supplementary Fig. 11**). Cell-free protein synthesis in the presence of droplets shows that droplets are highly biocompatible and will likely support many different biochemical reactions. Further, we can utilize this methodology as a rapid route to introduce functional proteins into the droplets to carry out specific biochemical transformations.

Programming partitioning behavior. Living cells and sub-cellular organelles contain specific receptors to recognize macromolecular binding partners or signaling molecules. For example, lysosomal enzymes synthesized in the rough ER are modified with mannose-6-phosphate for targeting them to lysosomes[42]. Since our droplets are composed of amphiphilic species, we asked if such targeting mechanisms could be mimicked by doping the droplets with amphiphiles bearing affinity handles. At first, we doped the droplets with 11.3 mol% *N*-oleoyl β-D-mannopyranosylamine (MOA) and added fluorescein isothiocyanate (FITC) labeled lectin Concanavalin A, which has specificity for terminal mannopyranosyl residues. As expected, we observed that the droplets doped with MOA had a 1.14-fold higher fluorescence signal compared to the background while those without did not show increased fluorescence (**Fig. 2d**). Encouraged by this result, we doped the droplets with 1.6 mol% 1,2-dioleoyl-*sn*-glycero-3-[(*N*-(5-amino-1-carboxypentyl) iminodiacetic acid) succinimidyl] (nickel salt) (Ni-NTA-DGS) – a headgroup modified phospholipid that binds to polyhistidine-tagged proteins with high affinity and specificity. When we added sfGFP-His$_6$, we observed highly efficient localization using confocal microscopy. In absence of Ni-NTA-DGS, no localization of sfGFP-His$_6$ was observed (**Fig. 2e**). To further quantify how much sfGFP-His$_6$ partitioned into Ni-NTA-DGS-doped droplets, we analyzed droplet supernatants fluorometrically. Droplets sequestered more than 90% of the protein when we titrated sfGFP-His$_6$ between 1 nM and 10 µM (**Supplementary Fig. 12**). At 10 µM total sfGFP-His$_6$ concentration, we estimate the protein concentration to be almost 1 mM in the droplet phase, based on droplet formation experiments at comparable GOA and IGEPAL concentrations in large volumes, where the droplets phase occupied approximately 1% of the total volume. Our calculations indicate that His-tagged proteins in the droplet phase can therefore easily reach the concentrations of even the most abundant proteins in cells (for instance, the translation elongation factor EF-Tu is present at approximately 100 µM in *E. coli*)[23]. The capacity of droplets for sequestering His-tagged protein obviously depends on the density of droplets and the amount of Ni-NTA-DGS, which explains why partitioning saturates as the protein concentration approaches the concentration of Ni-NTA-DGS (**Supplementary Fig. 12**). Next, we doped the droplets with 10 mol% of the cationic amphiphile cetyltrimethylammonium bromide (CTAB) and found that it facilitated the sequestration of a fluorescently labeled oligonucleotide (5′-FAM dN$_{20}$) (**Fig. 2f**). We measured the fluorescence signal in the droplets to be 1.2-fold higher than the background when 2 µM 5′-FAM dN$_{20}$ was added to CTAB-doped droplets, while no increase was observed in non-doped droplets. Doping with a biotinylated phospholipid (biotinyl-PE) allowed us to recruit fluorescently labeled Streptavidin into the sponge phase, where the protein was concentrated more than 10-fold from solution (**Fig 2g**). Recruitment of streptavidin suggests that additional biotinylated molecules may be co-sequestered when bound to streptavidin tetramers.

Mobility of molecular cargo in lipid sponge droplets. For reactions to occur in a synthetic organelle model, it is important that molecules are mobile within the compartment. As mentioned earlier, the spherical shape suggests that the droplets are liquid in nature. Additionally, we frequently observe fusion events between individual droplets that coalesce into a bigger droplet (**Supplementary Video 2**). To quantify the mobility of molecules inside droplets, we performed fluorescence recovery after photobleaching (FRAP) experiments (**Supplementary Fig. 13**). To study the mobility of hydrophobic molecules, we bleached the center of a droplet containing a fluorescently labeled phospholipid and the half-maximal recovery of fluorescence was observed within 6.8 s ($t_{1/2}$). To study the mobility of soluble proteins, we carried out FRAP on Ni-NTA-DGS-doped droplets binding a His$_6$-tagged fluorescent protein and measured a $t_{1/2}$ of 16 s. As controls, we compared protein diffusion in droplets to the mobility of the protein in aqueous water-in-oil

emulsion droplets and bound to a Ni-NTA gel matrix, where, respectively, fluorescence recovery was much more rapid or did not occur over the duration of the experiment (**Supplementary Fig. 13**). The FRAP results indicate that molecular cargo within the droplet phase diffuses slower than in a dilute aqueous solution but they are sufficiently mobile to allow dynamic molecular interactions to occur.
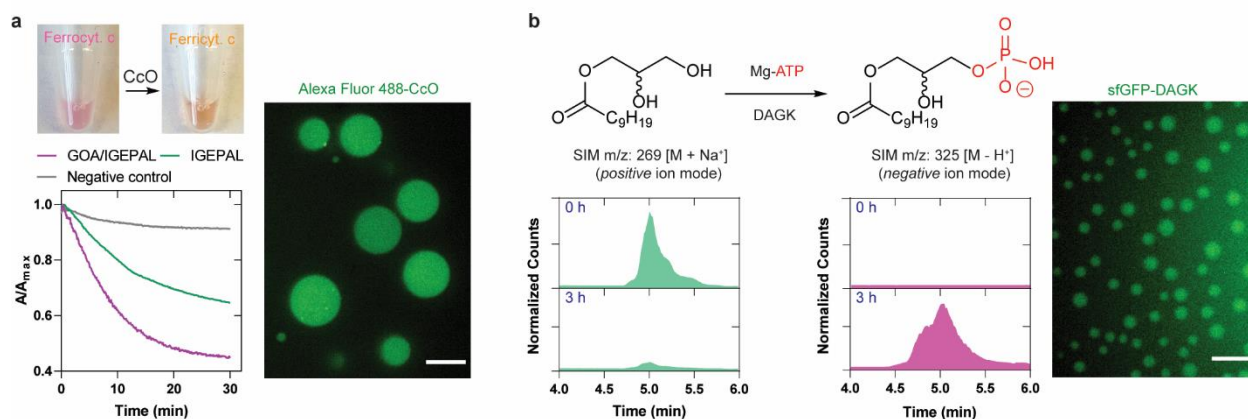

Fig. 3 | Reconstitution of functional transmembrane proteins. **a**. Cytochrome c oxidase (CcO) reaction. Addition of ferrocytochrome c to a droplet dispersion containing CcO leads to a gradual decrease in the absorbance at 550 nm indicating the formation of ferricytochrome c. Alexa Fluor 488-labeled CcO partitions into the droplets. Scale bar: 10 μm. **b**. *E. coli* diacylglycerol kinase (DAGK) reaction in droplets. DAGK is expressed in PURE system in the presence of droplets containing the substrate 1-decanoyl-*rac*-glycerol. Selective ion monitoring (SIM) chromatogram shows transformation to the phosphorylated product. Similarly expressed fluorescent fusion protein sfGFP-DAGK partitions into the droplets. Scale bar: 5 μm.

Reconstitution of functional transmembrane proteins. Membrane proteins are encoded by a large proportion (~30%) of the genome and they fulfill essential cellular functions[26]. However, they are challenging to employ in systems built from the bottom up, limiting the range of biochemical transformations that can be implemented in cell-free reactions. Since the droplets are composed of biocompatible lipid bilayers, we were interested in testing if spontaneous reconstitution of transmembrane proteins was possible. As a proof of concept demonstration, we chose commercially available cytochrome c oxidase (CcO) solubilized in *n*-dodecyl-*β*-D-maltoside (DDM) as a model integral membrane protein. CcO is a large transmembrane protein complex found in the inner mitochondrial membrane and it is the terminal enzyme of the respiratory electron transport chain. Initially, we exchanged DDM with IGEPAL using spin filtration. Next, we prepared the droplets by hydrating a GOA film in the presence of IGEPAL-solubilized CcO. When ferrocytochrome c was added to the droplets, we observed a steady decrease in absorbance at 550 nm indicating the enzyme-catalyzed formation of ferricytochrome c (**Fig. 3a**). In comparison, when the activity was measured with IGEPAL-solubilized CcO only, a two-fold lower reaction rate was observed. The bilayer membrane environment within the droplets likely allowed proper folding and membrane insertion of CcO in comparison to solubilization in IGEPAL only. In addition, it may be possible that the lipid environment of the droplets led to increased solubility of molecular O_2, the electron acceptor in the reaction, and hence an increased reaction rate. Finally, for direct observation, we labeled CcO with Alexa Fluor 488, and observed spontaneous partitioning into the droplets (**Fig. 3a**).

Membrane proteins of the endomembrane system participate in a variety of transformations of lipid substrates. The ER contains the biosynthetic machinery for the production of phospholipids and steroids[43]. Comparably packed with membrane bilayer networks and with their ability to sequester membrane proteins and hydrophobic molecules, sponge droplets may offer an excellent environment for reactions involving lipid substrates. To test our hypothesis, we expressed bacterial (*E. coli*) diacylglycerol kinase (DAGK), a 13.2 kDa protein containing three transmembrane helices, in a PURE TX-TL reaction in the presence of droplets. DAGK catalyzes the phosphorylation of diacylglycerols and monoacylglycerols. The droplets were doped with 9.1 mol% 1-decanoyl-*rac*-glycerol, a substrate for DAGK, and additional ATP and $MgCl_2$ were added in the reaction mixture to support phosphorylation activity. After 3 h, the expected product decanoyl lysophosphatidate could be detected in nearly quantitative conversion as evidenced by the mass spectrometric signals (**Fig. 3b**). To visualize the partitioning of the protein into the droplets, we expressed sfGFP-fused DAGK in the TX-TL system and observed fluorescence signal in the droplets indicating localization of the expressed protein (**Fig. 3b**). Our results demonstrate that droplets can facilitate an important enzymatic step in the biosynthesis of phospholipids. In the future, lipid sponge droplets, with their high membrane density and large lipid-aqueous interface, could provide a platform for reconstituting more complex biochemical pathways involving multiple transmembrane proteins. In particular, we believe there is potential for the reconstitution of lipid biosynthesis pathways to emulate and characterize functions of the smooth ER.

Rate enhancement of enzymatic reactions in the droplets. Living cells use organelles to co-localize molecules to facilitate reactions and minimize unwanted side reactions. Using compartmentalization to enhance biochemical reaction rates in living cells has been demonstrated by synthetic biologists and metabolic engineers. For instance, confinement of enzymatic pathways and key intermediates in mitochondria of engineered yeast has been shown to increase metabolite titer significantly as compared to cytoplasmic pathways[44]. Similar strategies have been employed to enhance the yield of fatty acid-derived metabolites in yeast peroxisomes[45]. We asked if colocalization of an enzyme and its substrate in droplets would enhance the rate of a biochemical reaction. First, we bound His_6-tagged cathepsin K, a lysosomal cysteine protease, within Ni-NTA-DGS doped droplets (**Fig. 4a**). Next, we added a fluorogenic dipeptide substrate benzyloxycarbonyl-L-leucyl-L-arginine 7-amido-4-methylcoumarin (Z-LR-AMC), which gets sequestered within droplets by virtue of its partial hydrophobic nature (**Fig. 4a**). We monitored the progress of the cathepsin K catalyzed hydrolysis reaction by measuring the steadily increasing fluorescence signal from the by-product 7-amino-4-methylcoumarin (AMC) (**Fig. 4b**). We observed that the progress of reaction was markedly higher when compared to the bulk phase reaction in the absence of droplets. We performed additional control reactions where we (i) omitted Ni-NTA-DGS from the droplets (non-binding droplets), and (ii) used IGEPAL only, and in each case, we found that the increase in AMC fluorescence signal was lower than the condition where both enzyme and substrate were co-localized in the droplets. We further corroborated and quantified these results by measuring the amount of AMC generated using HPLC-MS based on standard calibration curves (**Supplementary Fig. 14**). We estimated that after 6 hours, 84.7% of Z-LR-AMC was hydrolyzed in the binding droplets (**Fig. 4c**). In the presence of non-binding droplets or IGEPAL alone, 25.7% and 18.6% of Z-LR-AMC was hydrolyzed respectively. Only 2.5% of Z-LR-AMC was hydrolyzed in the bulk condition. A likely explanation for the higher yield of product in the non-binding droplets and IGEPAL only conditions compared to the bulk without additives is that the amphiphiles facilitated dispersal of the substrate in the reaction media.

10

Nonetheless, the product yield is enhanced greatly by programming the droplets to sequester cathepsin K and by concentrating and co-localizing enzyme and substrate. We believe that the droplets will offer a general scaffold for studying the effects of colocalization and confinement on enzymatic reactions.
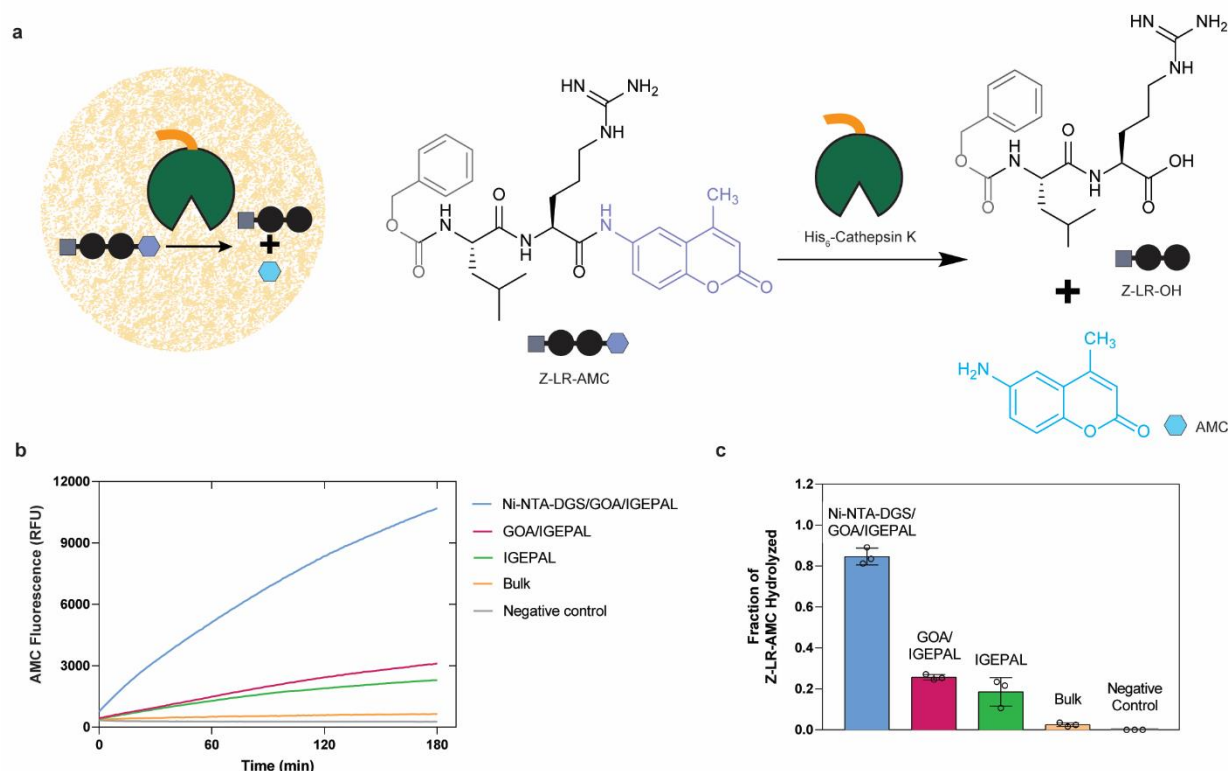

Fig. 4 | Rate enhancement of a model biochemical reaction due to co-localization of an enzyme and its substrate. **a**. Reaction scheme showing hydrolysis of a fluorogenic dipeptide Z-LR-AMC catalyzed by His$_6$-Cathepsin K. **b**. Progress of hydrolysis of Z-LR-AMC in droplets and corresponding controls followed by fluorometry. **c**. Quantification of the extent of hydrolysis of Z-LR-AMC in droplets and corresponding controls by HPLC-MS.

Light-controlled protein encapsulation. In living cells, proteins often shuttle dynamically between different subcellular locations in response to changes in the environment. For example, transcription factors shuttle between the nucleus and the cytoplasm, and cells dynamically alter the number of signaling receptors in the plasma membrane by endocytosis[46]. Furthermore, cells regulate the availability of signaling proteins by forming and dissolving membraneless compartments such as stress granules in response to environmental factors[1]. Sequestration of proteins into intracellular phase separated droplets has also been engineered to be responsive to light stimuli[47]. We aimed to engineer light-controlled and reversible protein sequestration into lipid sponge droplets. The photoreceptor phytochrome B (PhyB) from *Arabidopsis thaliana* switches between a binding and a non-binding conformation upon exposure to red (660 nm) and far-red (740 nm) wavelengths respectively (**Supplementary Fig. 15**). In its binding conformation, PhyB binds to phytochrome interacting factors (PIFs) that can be fused to cargo proteins[48]. We used this system to control the capture and release of proteins by droplets with light. PhyB was

11

produced with a biotin affinity handle, bound to Streptavidin and encapsulated in droplets doped with biotinyl-PE (**Fig. 5a**). PhyB-loaded droplets encapsulated PIF-sfGFP-ssrA after exposure to daylight or 660 nm light. The protein was not enriched in droplets in 740 nm light or in the absence of PhyB (**Fig. 5b, Supplementary Fig. 16**). Alternating exposure of droplets with red and far-red light reversibly switched the localization of PIF-sfGFP-ssrA between droplets and solution. Release and capture of the protein was rapid. Droplets lost 90% of GFP fluorescence within 2-3 min after switching illumination to 740 nm far-red light, and fluorescence signal from the solution in the vicinity of droplets increased immediately. When droplet samples were illuminated with 660 nm light, fluorescence signal from the solution decreased and fluorescence of droplets began to increase. Fluorescence of PIF-sfGFP-ssrA was observed to spread from the edges into the interior of droplets. In large droplets with diameters of more than 40 μm it took more than 30 min to reach a homogeneous intensity of GFP from droplet edge to interior (**Fig. 5b, Supplementary Video 3**). The observed differences in the release and binding speeds can be explained by the differences in PIF-tagged protein concentration under the different illumination conditions in droplets and solution respectively. Sequestration into droplets is slower than release because the protein is at a relatively low concentration in solution, and sequestration into the droplets only occurs after an encounter of a PIF-tagged protein in solution and a droplet-bound PhyB. Light controlled localization changes were readily reversible and could be observed for more than 6 h. The observed fast release kinetics will be useful to rapidly make proteins available for reaction in solution.

Light-controlled sequestration in droplets reversibly protects from degradation. Cells utilize a "nucleolar detention" strategy to regulate molecular networks by capturing and immobilizing essential cellular factors within the nucleolus away from their effector molecules[49]. We reasoned that light-controlled protein release and capture by droplets should allow us to control reactions in a similar manner. In contrast to the previous reactions that we engineered to occur within droplets, we focused on a reaction happening in solution, outside of droplets: ClpXP mediated protein degradation. ClpXP (from *E. coli*) is a large protein complex of approximately 600 kDa that consists of 6 ClpX and 14 ClpP subunits. ClpXP degrades ssrA-tagged protein substrates in a highly specific, processive and ATP-dependent manner and has a K_M of about 500 nM for ssrA-tagged sfGFP[50]. Since this protein complex has a cylindrical shape of 14.5 nm length and 11 nm diameter[51], which are significantly larger than the average channel diameter of 4.1 nm, we expect it to be excluded from the droplets. Indeed we observe that ClpP-msfGFP-His$_6$ is excluded from biotinyl-PE-doped droplets and cannot enter the droplets even when targeted inside using Ni-NTA-DGS (**Fig. 5a, Supplementary Fig. 17**). Light-controlled changes in PIF-sfGFP-ssrA concentration in solution should therefore affect the rate of proteolytic degradation of the protein by ClpXP. As predicted, we found that in 660 nm illumination conditions degradation of PIF-sfGFP-ssrA was substantially slower than in 740 nm illumination conditions in the presence of PhyB-loaded droplets. We observed differences in degradation rate by fluorometric measurements of the reaction over time (**Fig. 5c, Supplementary Fig. 18**). We further corroborated these data by microscopy of reaction samples, and immunoblotting (**Supplementary Figs. 19-20**). The light-dependent behavior allowed us to dynamically control the degradation rate by changing the illumination wavelength. Switching illumination between 660 nm and 740 nm led to pronounced and immediate changes in degradation rate (**Fig. 5c**). Protection from ClpXP-mediated degradation required the presence of PhyB-loaded droplets. The Streptavidin-PhyB complex alone, without droplets, slowed degradation only marginally. Also, in the presence of droplets without PhyB, no protection or responses to wavelength changes were

observed. In the absence of ClpXP, GFP signal decreased only marginally (**Supplementary Fig. 18**). As shown here for light-switchable protection of a sequestered protein from degradation in solution, light-responsive droplets will enable precise spatiotemporal control of reactions both in solution and in the droplet phase.
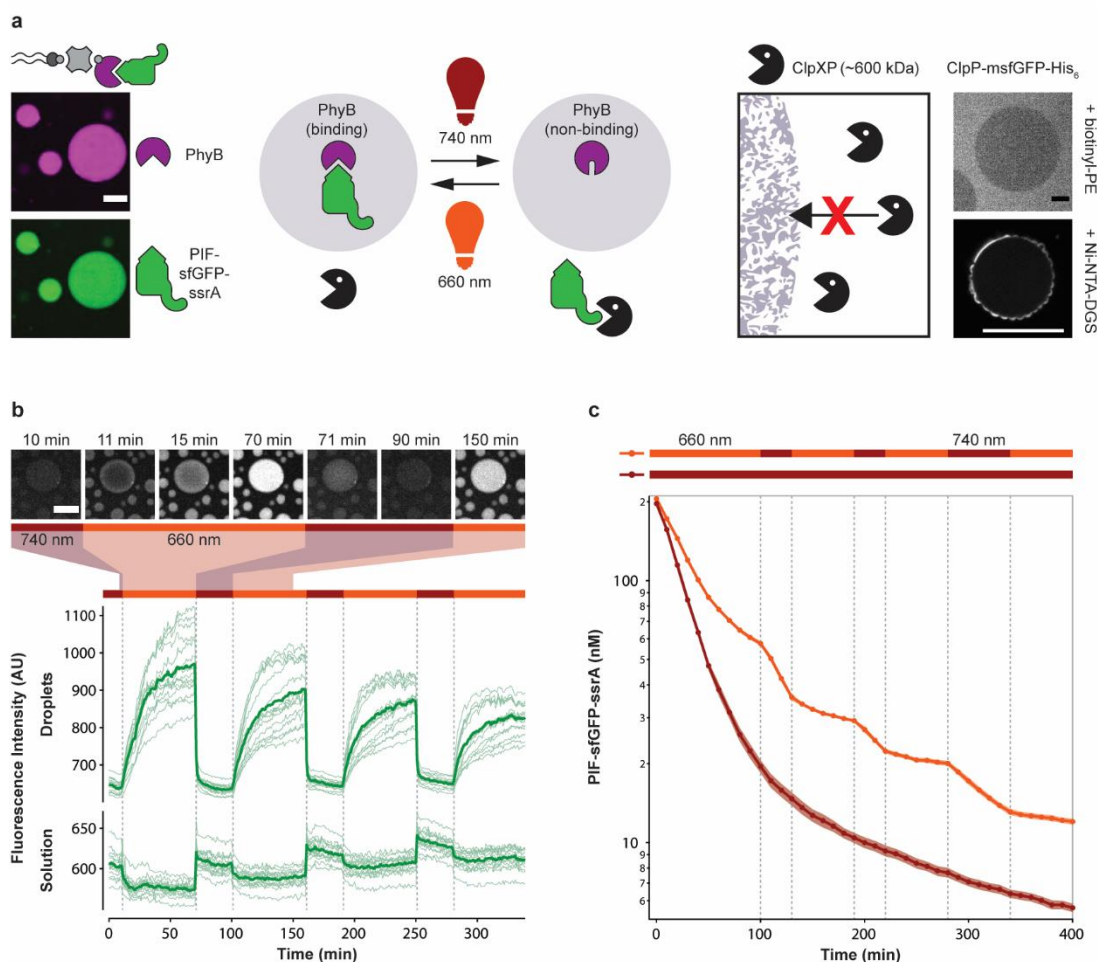

Fig. 5 | Light-dependent protein capture and release to dynamically control degradation rates. a. Design of the light-controlled protein degradation reaction. Left: Biotin-Streptavidin-mediated binding of light-responsive phytochrome B (PhyB) and capture of the protease substrate PIF-sfGFP-ssrA in 660 nm light. Right: Exclusion of ClpXP protease from lipid sponge droplets. ClpP-msfGFP-His$_6$ is excluded from droplets doped with biotinyl-PE and is unable to enter droplets when targeted inside via Ni-NTA-DGS. **b**. Light-controlled release and capture of PIF-sfGFP-ssrA by PhyB-loaded droplets. Traces show fluorescence intensities of droplets and solution over time in response to changing illumination conditions. Bars above indicate 660 nm and 740 nm conditions. Intensities were extracted from a total of 15 droplets in 5 time-lapse movies (thin lines) and averaged (bold lines). Selected images from a time-lapse movie are shown on top. **c**. Light-controlled switching between protection and degradation of PIF-sfGFP-ssrA by ClpXP. Degradation of PIF-sfGFP-ssrA was monitored by reading the fluorescence of the reaction every 10 min. Reactions were performed in triplicates. Shown is the average (bold) and the standard deviation (shaded areas). Scale bars: 20 µm.

Conclusion

In summary, we describe the application of lipid sponge droplets as mimics of membrane-rich organelles and subcellular structures. With their nanoporous structure offering abundant hydrophobic-hydrophilic interfaces, the droplets spontaneously sequester molecules from the surrounding medium based on their physico-chemical properties. Further, the droplets are programmable in a modular fashion using amphiphiles with affinity handles that specifically target tagged proteins into the sponge phase at high concentrations. This is a significant advantage over vesicle-based artificial organelle models, which suffer from the limitation that they have no mechanism for efficient and spontaneous internal sequestration of macromolecules and solutes. Being composed of biocompatible building blocks, the lipid sponge droplets support a wide range of enzymatic reactions catalyzed by both transmembrane and soluble proteins and involving both water soluble and lipophilic substrates. Furthermore, we showed that a combination of colocalization, increased concentration, and the molecularly crowded environment can enhance enzymatic reactions in the droplets. The open and liquid nature of the droplets allows exchange with the surrounding environment, as well as reversible, light-responsive control over protein localization and concentration, which is difficult to engineer in a vesicle-based artificial organelle. Due to their versatile, self-assembled, and programmable nature lipid sponge droplets will find application as organelle-mimics to spatially organize biochemical reactions within artificial cellular systems and in cell-free systems. Finally, alternative, non-vesicular lipid structures such as the one reported here could serve as additional models for protocellular evolution. Fatty acid vesicles, which are popular protocell models, have been shown to transform to coacervates under certain conditions[37]. Interconversion or coexistence of such structures may have important implications in protocellular structural diversity, stability, and permeability and deserves further exploration.

Methods

HPLC-MS. Solvent mixtures for chromatography are reported as volume/volume (v/v) ratios. HPLC analyses were carried out on an Eclipse Plus C8 analytical column with *Phase A*/*Phase B* gradients [*Phase A*: H_2O with 0.1% formic acid; *Phase B*: MeOH with 0.1% formic acid]. HPLC purification was carried out on Zorbax SB-C18 semipreparative column with *Phase A*/*Phase B* gradients [*Phase A*: H_2O with 0.1% formic acid; *Phase B*: MeOH with 0.1% formic acid]. Electrospray Ionization-Mass spectra (ESI-MS) were obtained on an Agilent 6230 Accurate-Mass Time of Flight (TOF) mass spectrometer.

Microscopy. Spinning-disk confocal microscopy images were acquired on a Yokagawa spinning-disk system (Yokagawa, Japan) built around an Axio Observer Z1 motorized inverted microscope (Carl Zeiss Microscopy GmbH, Germany) with a 63x, 1.40 NA oil immersion objective or 20x 0.8 NA objective to an ORCA-Flash4.0 V2 Digital CMOS camera (Hamamatsu, Japan) using ZEN Blue imaging software (Carl Zeiss Microscopy GmbH, Germany). The fluorophores were excited with diode lasers (405 nm-20 mW, 488 nm-30 mW, 561 nm-20 mW, and 638 nm-75 mW). A condenser/objective with a phase stop of Ph3 was used to obtain the phase-contrast images with a 100x objective on an Olympus BX51 microscope.

Synthesis of glycolipids. All glycolipids described in this study were synthesized based on a small variation of previously published procedure[33]. A solution of 1 equivalent of the unsaturated fatty acid and 1.1 equivalents of *N, N*-diisopropylethylamine (DIPEA) in dimethylformamide (DMF) was stirred at 0 ºC for 10 min, and then 1.1 equivalents of 1-[Bis(dimethylamino)methylene]-1*H*-

14

1,2,3-triazolo[4,5-*b*] pyridinium 3-oxide hexafluorophosphate (HATU) (1.1 equivalents) was added. After 10 min stirring at 0 ºC, 1 equivalent of β-D-glycopyranosylamine was added. After stirring for 1 h at room temperature, the solvents were removed *in vacuo* to obtain a yellow residue. This was washed with cold dilute HCl. The resulting off-white crude is dissolved in methanol and the slightly yellow solution is filtered using a 0.2 μm syringe-driven filter and purified by HPLC (Zorbax SB-C18 semipreparative column, 5% *Phase A* in *Phase B*, 6.5-7.5 min). The purified glycolipids are obtained as white powders.

Droplet formation. Typically, 9 μL of GOA from a 10 mM stock solution in methanol were added to 50 μL chloroform in a glass vial. When droplets were doped with amphiphiles bearing affinity handles, stock solutions were prepared in methanol and added into the chloroform as well. The organic solvents were evaporated under a slow stream of nitrogen gas and, while carefully rotating the glass vial, a thin film was generated at the bottom of the vial. The film was hydrated with a solution containing different amounts of IGEPAL (Sigma I8896, Lot # MKCC9036) within the droplet forming composition range (**Fig. 1d**) as indicated for each experiment. The vial was vortex mixed until the lipid film was completely resuspended and the dispersion appeared turbid. To ensure complete hydration of the film, the sides and bottom of the vial are scratched with the pipette tip. As droplets form robustly at different GOA and IGEPAL concentrations and in different buffer compositions, the volume and composition of the rehydration solution was adjusted as indicated for each experiment.

Thermogravimetric analysis. A droplet dispersion was prepared in MilliQ H_2O from 3 mM GOA and 2.25 mM IGEPAL and allowed to coalesce into a single phase. The coalesced phase (2.351 mg) was carefully collected from the bottom of the tube and loaded onto a ceramic crucible. Thermogravimetric analysis was carried out on a Perkin-Elmer STA 6000 Simultaneous Thermal Analyzer. The sample was heated at 10 °C/min over the range 30-350 °C. Nitrogen gas flow was maintained at 20 mL/min. We present the data over the range 30-150 °C. Above ~200 °C, the residual materials underwent thermal decomposition (data not shown).

Cryogenic Transmission Electron Microscopy (Cryo-TEM). Sponge droplets were prepared from 3 mM GOA and 2.25 mM IGEPAL and sonicated with heating to ensure formation of small droplets. Immediately before grid preparation, the droplet sample was pipetted onto plasma-cleaned 300-mesh Quantifoil Multi-A carbon grids (Quantifoil). Using a Vitrobot EM grid plunger (FEI), excess buffer was blotted at room temperature and 95% humidity and the grids were plunge-frozen in liquid ethane maintained at about -180 °C. The grids were stored in liquid nitrogen until use. Droplet samples were imaged on a JEM-2100F microscope (JOEL) fitted with a OneView 4K charge-coupled device camera (Gatan).

Cryogenic Scanning Electron Microscopy (Cryo-SEM). Approximately 3 μL of sample (dispersion of 3 mM GOA and 2.25 mM IGEPAL) was pipetted onto a 3 mm Al planchette and flash frozen in liquid ethane before loading into a Leica cryo-transfer shuttle for insertion into a Leica ACE600 cooled down to -130 °C. The sample was then freeze-fractured and freeze-etched for 6 minutes at -105 °C and coated with 7 nm of C/Pt and an additional 5 nm of C. The sample was then transferred to in a Hitachi S-4800 cFEG-SEM fitted with a Leica cryo-stage cooled down to -130 °C. Imaging occurred at 5 kV with an approximate working distance of 9.7 mm.

Small-angle X-ray scattering (SAXS). For studying the sponge phase characteristics, we prepared a series of samples with controlled ratios between GOA and IGEPAL. The droplet dispersions were loaded in thin walled (0.01 mm) special glass capillary tubes of 15 mm outer diameter (15-SG, Charles Supper Company). Synchrotron X-ray scattering measurements were performed at the Advanced Photon Source (APS), Argonne National Laboratory (ANL) at

beamline 12-ID-C with monochromatic photon flux 1 x 10^{13} photons/s/cm^2. A focused beam of dimension 1 × 1 mm^2 with incident photon energy at 18 keV (wavelength = 0.69 Å) was employed with exposure times of 10 s to get a reasonable scattering signal from the sample. The SAXS data were collected by a CCD detector (2048 x 2048 pixels) and the sample-to-detector distance was 3825 mm. To obtain one-dimensional SAXS profiles, 2-dimensional scattering data were azimuthally averaged with proper background subtraction. Finally, the data were transformed into the profiles of scattering intensity as a function of scattering vector (q).

Sequestration experiments. All droplet dispersions for the sequestration experiments were prepared from 3 mM GOA and 2.25 mM IGEPAL such that the total mass of droplet forming amphiphiles was 80 µg. 5 µg of the molecule to be sequestered were added in each case. In case of sequestration studies of fluorescein, POPC, and cholesterol, 5 µL of 1 mg/mL solution in EtOH were added during GOA film formation. 20 µL of the cloudy droplet dispersion was collected in a 0.6 mL Eppendorf tube and placed in an incubator at 37 °C for 2 h. The tubes were centrifuged at 14,000 rcf for 2 min to ensure complete coalescence of the droplets. 2 µL of the supernatant was collected carefully and diluted with 98 µL 1:1 MeOH: H$_2$O. This was injected as whole into HPLC-MS and the peak area corresponding to the analyte in consideration was measured (denoted by S). The coalesced phase was resuspended by vigorous vortexing and 2 µL of the dispersion was diluted with 98 µL 1:1 MeOH: H$_2$O. This was injected as whole into HPLC-MS and the peak area corresponding to the analyte in consideration was measured (denoted by T). The sequestered fraction was calculated from the following equation:

$$Fraction\ Sequestered = 1 - S \div [S \times 0.1 + T \times 0.9]$$

The experiments were carried out in triplicate and the combined data are presented in **Supplementary Table 1**.

Sequestration of LecA (PA-IL). *Fluorescent labeling of LecA.* Terminal galactose-binding lectin LecA (or PA-IL) from *Pseudomonas aeruginosa* was purchased from Sigma-Aldrich. 0.31 mg of the solid powder (~80% protein) was dissolved in 200 µL 100 mM NaHCO$_3$, pH 8.3. 3.3 equivalents of Alexa Fluor 488 NHS ester (dissolved in anhydrous DMSO) was added to this solution, and the mixture was stirred at room temperature for 2 h. The excess dye was removed by a commercial dye removal kit (Pierce, Thermo Fisher Scientific). The eluent was further washed and exchanged with 1X PBS using a 10 kDa MWCO spin filter and stored at -20 °C as 10% glycerol stock containing 0.02% (*w/v*) NaN$_3$.
Microscopic observations. GOA droplets were prepared with 3 mM GOA and 1.33-2.25 mM IGEPAL. Sequestration of various concentrations of Alexa Fluor 488 labeled LecA (1.0 µM-0.25 nM) was studied by spinning disk confocal microscopy.

Reconstitution of Cytochrome c Oxidase (CcO). *Reduction of ferricytochrome c.* 1.72 mg of reddish-brown powder of ferricytochrome c from bovine heart (Sigma) were dissolved in 190 µL PBS (1X). Then, 10 µL of sodium ascorbate (200 mM) were added. The mixture was kept at 4 °C overnight, observing that its color changed to rose-red. The residual ascorbate was removed by dialysis (mini dialysis device, 10 kDa MWCO, Slide-A-Lyzer^{TM}) against 10 mM sodium phosphate buffer (pH 7.0) followed by spin filtration using a 10 kDa MWCO spin filter with 6X volume. The final concentration of ferrocytochrome c was determined to be 1.11 mM and the A$_{550}$/A$_{565}$ ratio was 17.43.
Detergent exchange of CcO. 5 µL of CcO from bovine heart (~5 mg/mL in 39 mM DDM, 25 mM Tris pH 7.8, 5 mM EDTA) was added to 197.5 µL (in 10 mM sodium phosphate buffer, pH 7.0) of 1.68 mM IGEPAL. 2.5 µL of this solution was dissolved in 97.5 µL MeOH and mixed by vigorous vortexing. The tube was centrifuged at maximum speed to remove any insoluble material. The

supernatant was carefully collected and run on HPLC-MS and the peaks corresponding to DDM and IGEPAL were seen distinctly. The remaining solution was transferred to a 100 kDa MWCO spin filter and thoroughly washed with (5×200 µL) of 1.68 mM IGEPAL (in 10 mM sodium phosphate buffer, pH 7.0). 1 µL of the final retentate (~35 µL) was added to 99 µL MeOH and run on HPLC-MS as described. The analysis verified that the DDM present in the commercially available CcO was completely exchanged with IGEPAL. Based on a calibration curve, the concentration of IGEPAL was estimated to be 18.8 mM.

Activity assay of CcO. A lipid film from 39 µL of 10mM GOA was hydrated with a solution containing 377 µL sodium phosphate (10 mM, pH 7.0), 6 µL CcO (in 18.8 mM IGEPAL and 10 mM sodium phosphate pH 7.0), and 7 µL of IGEPAL (16 mM in 10 mM sodium phosphate pH 7.0). The turbid droplet dispersion was transferred to a cuvette and 15 µL of ferrocytochrome c was added. The dispersion was mixed by tapping and pipetting and placed in Nanodrop 2000c. Absorbance at 550 nm was measured every 5 s over 30 min and a steady decrease was observed.

To compare the activity of CcO in same concentration of IGEPAL in absence of the droplets, a sample was prepared in an identical manner and the activity was assayed.

A negative control sample was prepared and assayed where no CcO was added. The A_{550} was recorded identically and a negligible decrease was observed.

Fluorescent labeling of CcO. 60 µg of commercially available CcO from bovine heart (Sigma) was exchanged with sodium bicarbonate buffer (100 mM, pH 8.3) containing 0.4 mM *n*-dodecyl-*β*-maltoside (DDM). Then, the solution was treated with 10 equivalents of Alexa Fluor 488 NHS ester (dissolved in anhydrous DMSO), and the mixture was stirred at room temperature for 2 h. Then, the excess dye was removed and DDM was exchanged with IGEPAL by spin filtration (100 kDa MWCO).

Activity of Cathepsin K in droplets. *General.* Recombinant His_6-tagged Human Cathepsin K was purchased from EMD Millipore. The enzyme was stored as 18.5 µM aliquots in 100 mM NaOAc/HOAc buffer (pH 5.5) containing 1 mM TCEP at -80 °C. The protein was labeled with Alexa Fluor 488 and microscopy verified its sequestration into droplets doped with Ni-NTA-DGS. Benzyloxycarbonyl-L-leucyl-L-arginine 7-amido-4-methylcoumarin (Z-LR-AMC) was purchased from Peptides International and stored as 10.8 mM DMSO solution at -80 °C. It was estimated from HPLC that 75% of Z-LR-AMC gets partitioned to the droplets used in the subsequent experiments.

Fluorometric assay. Ni-NTA-DGS/GOA/IGEPAL (26.7 µM/0.96 mM/0.64 mM) droplets were prepared in 100 mM HEPES-Na containing 1.5 mM TCEP. His_6-Cathepsin K was added to the droplet dispersion so that the enzyme concentration with respect to bulk was 2.3 nM. After incubating at room temperature for 10 min, Z-LR-AMC (dissolved in DMSO) was added such that the final concentration was 81 µM. Additional conditions were tested where one or more of the components were omitted: GOA/IGEPAL (0.96 mM/0.64 mM), IGEPAL (0.64 mM), bulk, and negative control (no amphiphiles and no enzyme). 20 µL of each sample was loaded onto a 384 well-plate and analyzed for fluorescence from 7-amino-4-methylcoumarin (λ_{ex}: 360 nm, λ_{em}: 460 nm; 10 nm bandwidth) every 1 min at room temperature in a Tecan Spark microplate reader.

HPLC-MS assay. Calibration curves were prepared for Z-LR-AMC and AMC with known quantities of the pure substances (**Supplementary Fig. 14**). Ni-NTA-DGS/GOA/IGEPAL (26.7 µM/0.96 mM/0.64 mM) droplets were prepared in 100 mM HEPES-Na containing 2.0 mM TCEP. His_6-Cathepsin K was added to the droplet dispersion to a bulk concentration of 2.8 nM. Z-LR-AMC was added to a final concentration of 81 µM. GOA/IGEPAL (0.96 mM/0.64 mM), IGEPAL (0.64 mM), bulk, and negative control (no amphiphiles and no enzyme) samples were also prepared in identical buffer and same quantity of enzyme (except for the negative control) and substrate were used. The reactions (20 µL) were incubated at room temperature for 6 h and quenched by addition of 80 µL of 1:1 MeOH:H_2O. The reactions were analyzed by HPLC-MS and

17

the areas of the peaks under 330 nm chromatogram were used for calculation of yields. The experiments were repeated in triplicate.

FRAP experiments. For the analysis of lipid diffusion, droplets were formed with 3.6 mM GOA, 2.56 mM IGEPAL and 36 µM Texas Red DHPE in 1X PBS. For the analysis of protein diffusion, droplets were formed with 3 mM GOA, 2.25 mM IGEPAL and 83 µM Ni-NTA-DGS in 100 mM HEPES pH 8. Purified mCherry-His$_6$ protein (Antibodies-online Inc.) was added to a final concentration of 10 µM. As controls, we performed FRAP experiments on mCherry-His$_6$ bound to Ni-NTA agarose resin (HisPur, Thermo Fisher Scientific) and a water-in-oil emulsion of 90 µM mCherry-His$_6$ in mineral oil containing 0.25% (*v*/*v*) Span-80. FRAP experiments were performed with a Zeiss Spinning Disk microscope using a 63x 1.4 NA oil objective. A circular region of interest (ROI) with a diameter of 9.6 µm was bleached in large droplets (>50 µm) with a 5 s pulse of the 561 nm laser at 100% intensity. Samples were imaged every 500 ms with a 150 ms exposure at 50% intensity. Movies were analyzed in Fiji/ImageJ to extract average fluorescence over time of the bleached ROI, entire droplet and background. Background corrected fluorescence values were used to correct for possible photobleaching

$$f(t) = \frac{F_{ROI}(t)}{F_{Whole}(t)}$$

and then scaled between 0 and 1

$$F(t) = \frac{f(t) - f(0)}{f(-10s) - f(0)}$$

where f(0) is the intensity at time 0s, right after the bleach, and f(-10s) is the initial prebleach intensity[52]. Data were then fitted to

$$F(t) = A(1 - e^{-\frac{t}{\tau}})$$

where A is the amplitude of recovery and τ is the time constant that allowed us to calculate the half-time to recovery $t_{1/2}$.

$$t_{1/2} = ln2 \cdot \tau$$

TX-TL in the presence of lipid sponge droplets. A lipid film was prepared from 18 µL 10 mM GOA and rehydrated by vortexing with 9 µL rehydration solution (6 µL PURExpress Solution A, 0.375 µL Murine RNase Inhibitor (NEB), 1.5 µL 67.3 mM IGEPAL, 1.125 µL H$_2$O). For the reaction to start, 4.5 µL PURExpress Solution B and linear DNA templates were added for a final volume of 15 µL. DNA template concentrations in the TX-TL reaction were 5 nM for P$_{T7}$-sfGFP-lecA and P$_{T7}$-sfGFP, and 10 nM for P$_{T7}$-sfGFP-lacI. Linear DNA templates were assembled by PCR and PCR purified, their sequences are listed in **Supplementary Table 2**. Expression reactions were carried out at 33 °C, in droplets of 5 µL volume sandwiched between cover glass and gas permeable Lumox plates (Sarstedt) or in chambers of a microfluidic device[53], where fluorescence increase of individual droplets could be followed by time lapse imaging. For expression of DAGK, a lipid film was prepared from 15 µL of 10 mM GOA and 3 µL of 10 mM 1-decanoyl-*rac*-glycerol (Cayman Chemicals). Hydration was carried out with 30 µL of a solution containing 5 mM IGEPAL, 0.5 mM ATP, and 0.5 mM MgCl$_2$. Protein expression reaction was consisted of 8 µL PURExpress Solution A, 6 µL PURExpress Solution B, 0.5 µL Murine RNase Inhibitor (NEB), 1 µL DAGK linear DNA (28.8 nM final concentration), 1 µL H$_2$O, and 4 µL droplet dispersion (containing the

18

substrates for DAGK). 10.25 µL of the reaction is taken out immediately and quenched with 4 µL Na_2-EDTA (100 mM) and 90 µL methanol. The remainder is incubated for 3 h at 37 °C and quenched similarly. The initial and final time points were analyzed by HPLC-MS in selective ion mode for m/z 269 (positive ion), and m/z 325 (negative ion). For the expression of sfGFP-DAGK, 13.4 nM of DNA template was used.

Protein expression, purification and analysis. Proteins (**Supplementary Table 2, Supplementary Fig. 21**) were expressed in *E. coli* BL21 (DE3) using the plasmids listed in **Supplementary Table 3**. ClpX-His$_6$ and ClpP-His$_6$ were gifts from Xingying Shi and Simpson Joseph (UC San Diego)[50]. Biotinylated PhyB(1-651)-AviTag with phycocyanobilin was produced in *E. coli*[48]. Proteins were purified by Ni-NTA affinity chromatography. Purified proteins were buffer exchanged to storage buffer using spin filter devices or dialysis. Storage conditions were 200 mM potassium phosphate pH 7.2, 2 mM EDTA, 400 mM NaCl, 1 mM DTT, 1 mM NaN$_3$, 50% (*v/v*) glycerol at -20 °C for sfGFP-LacI-His$_6$, 1X PBS at -80 °C for sfGFP-His$_6$, 100 mM HEPES pH 8.0, 25 mM NaCl, 0.5 mM TCEP, 50% (*v/v*) glycerol at -20 °C for PhyB-AviTag, 100 mM HEPES pH 8.0, 25 mM NaCl, 5 mM DTT, 50% (*v/v*) glycerol at -20 °C for His$_6$-PIF-sfGFP-ssrA, and 50 mM Tris pH 7.5, 200 mM KCl, 25 mM MgCl$_2$, 0.67 mM IGEPAL, 0.5 mM TCEP, 20% (*v/v*) glycerol at -80 °C for ClpP-msfGFP-His$_6$. Protein concentrations were measured by BCA assay. PhyB-AviTag was verified by Zinc staining to visualize the bound chromophore phycocyanobilin by incubating an SDS-PAGE gel in 1 mM zinc acetate for 15 min followed by visualization under UV light. Photoresponsive switching was verified by recording absorbance spectra of purified PhyB protein after exposure to 660 nm or 740 nm light using a Tecan Spark microplate reader. For immunoblotting, protein samples were separated by SDS-PAGE and transferred to PVDF membranes. Antibodies used were GFP Antibody (B-2) (Santa Cruz Biotechnology) at 1:200 and 6x-His Tag Monoclonal Antibody (Invitrogen) at 1:1000. Bands were detected with a horseradish peroxidase coupled secondary antibody and SuperSignal West Pico PLUS Chemiluminescent Substrate (Thermo Fisher Scientific).

ClpXP reactions. For light controlled protein degradation, droplets for one ClpXP reaction were prepared as follows, where the volumes were scaled according to the reactions performed in one experiment. Per reaction, a lipid film was formed from 7.2 µL 10 mM GOA and 0.8 µL 2.5 mM 18:1 Biotinyl-PE (Avanti). The lipid film was vortexed in 40 µL rehydration solution (1.35 mM IGEPAL in 100 mM HEPES pH 8.0) to form droplets. 40 µL of 2 µM Streptavidin and 2 µM PhyB-AviTag in reaction buffer [50 mM HEPES pH 8.0, 20 mM KCl, 5 mM MgCl$_2$, 1% (*v/v*) glycerol, 1% (*w/v*) BSA, 5 mM β-ME, 0.067 mM IGEPAL] were added and incubated with droplets for 15 min. Unbound PhyB and Streptavidin were then removed by washing with reaction buffer by pelleting droplets by centrifugation at 1500 rcf. During washing, droplets were concentrated in 10 µL reaction buffer, and the substrate PIF-sfGFP-ssrA was added for a final concentration of 250 nM in the reaction for binding to PhyB-loaded droplets and incubated for 15 min. The reaction was started by adding premixed ClpXP and ATP in reaction buffer (concentrations were 4 mM ATP, 50 nM ClpX$_6$, 200 nM ClpP$_{14}$ in a final reaction volume of 20 µL), and droplets were coalesced in the bottom of the reaction plate (384-well v-bottom plates, Promega) by centrifugation. The reaction was performed at room temperature, monitored by reading fluorescence of PIF-sfGFP-ssrA in a Tecan Spark microplate reader (excitation 485 +/- 20 nm (filter), emission 520 nm +/- 20 (monochromator)) every ten minutes and placed in specific illumination conditions between reads. For analysis by western blot, samples were collected at different time points, quenched by adding Laemmli buffer and stored at -20 °C. For analysis by microscopy, samples were first placed in 740 nm from 5 min and then in 660 nm light for 30 min to compare droplet fluorescence.

Light-control of protein localization. Samples were illuminated using LEDs (Roithner LaserTechnik GmbH, LED660N-03 and LED740-series) in light insulated containers, where LEDs were placed in proximity to samples using a custom-built setup. In 740 nm light conditions, samples were continuously illuminated by 740 nm light. In 660 nm light conditions, samples were illuminated every 10 min with a 30 s light pulse and otherwise incubated in the dark.

Acknowledgements

Author contributions

A.B., H.N., and N.K.D. conceived and designed the project. A.B., H.N., K.P., R.J.B, and C.H.T performed the biochemical, chemical, and imaging experiments. A.B., R.B., J.S., and S.K.S performed and analyzed the data for X-ray scattering experiments. A.B., H.N., and N.K.D wrote the manuscript.

Additional information

Any supplementary information, chemical compound information and source data are available in the online version of the paper. Correspondence and requests for materials should be addressed to N.K.D.

Competing interests

The authors declare no competing financial interests.

References

1. Hyman, A. A., Weber, C. A. & Jülicher, F. Liquid-Liquid Phase Separation in Biology. *Annu. Rev. Cell Dev. Biol.* **30,** 39–58 (2014).

2. Kiekebusch, D. & Thanbichler, M. Spatiotemporal organization of microbial cells by protein concentration gradients. *Trends Microbiol.* **22,** 65–73 (2014).

3. Simmel, F. C. Synthetic organelles. *Emerg. Top. Life Sci.* ETLS20190056 (2019).

4. Weiss, M., Frohnmayer, P. J., Benk, L. T., Haller, B., Janiesch, J-W., Heitkamp, T., Börsch, M., Lira, R. B., Dimova, R., Lipowsky, R., Bodenschatz, E., Baret, J-C., Vidakovic-Koch, T., Sundmacher, K., Platzman, I. & Spatz, J. P. Sequential bottom-up assembly of mechanically stabilized synthetic cells by microfluidics. *Nat. Mater.* **17,** 89–95 (2018).

5. Feng, X., Jia, Y., Cai, P., Fei, J. & Li, J. Coassembly of photosystem II and ATPase as Artificial chloroplast for light-driven ATP synthesis. *ACS Nano* **10,** 556–561 (2016).

6. Lee, K. Y., Park, S., Lee, K. H., Kim, S., Kim, H., Meroz, Y., Mahadevan, L., Jung, K., Ahn, T. K., Parker, K. K. & Shin, K. Photosynthetic artificial organelles sustain and control ATP-dependent reactions in a protocellular system. *Nat. Biotechnol.* **36,** 530–535 (2018).

7. Deng, N.-N., Yelleswarapu, M., Zheng, L. & Huck, W. T. S. Microfluidic Assembly of Monodisperse Vesosomes as Artificial Cell Models. *J. Am. Chem. Soc.* **139,** 587–590 (2017).

8. Hindley, J. W., Elani, Y., McGilvery, C. M., Ali, S., Bevan, C. L., Law, R. V. & Ces, O. Light-triggered enzymatic reactions in nested vesicle reactors. *Nat. Commun.* **9,** 1093 (2018).

9. Nakashima, K. K., Vibhute, M. A. & Spruijt, E. Biomolecular chemistry in liquid phase separated compartments. *Front. Mol. Biosci.* **6,** 21, (2019).

10. Poudyal, R. R., Guth-Metzler, R. M., Veenis, A. J., Frankel, E. A., Keating, C. D. & Bevilacqua, P. C. Template-directed RNA polymerization and enhanced ribozyme catalysis inside membraneless compartments formed by coacervates. *Nat. Commun.* **10,** 490 (2019).

11. Sokolova, E., Spruijt, E., Hansen, M. M. K., Dubuc, E., Groen, J., Chokkalingam, V., Piruska, A., Heus, H. A. & Huck, W. T. S. Enhanced transcription rates in membrane-free protocells formed by coacervation of cell lysate. *Proc. Natl. Acad. Sci.* **110,** 11692–11697 (2013).

12. Koga, S., Williams, D. S., Perriman, A. W. & Mann, S. Peptide-nucleotide microdroplets as a step towards a membrane-free protocell model. *Nat. Chem.* **3,** 720–724 (2011).

13. Aumiller, W. M. & Keating, C. D. Phosphorylation-mediated RNA/peptide complex coacervation as a model for intracellular liquid organelles. *Nat. Chem.* **8**, 129–137 (2016).

14. Deng, N. N. & Huck, W. T. S. Microfluidic Formation of Monodisperse Coacervate Organelles in Liposomes. *Angew. Chem. Int. Ed.* **56,** 9736–9740 (2017).

15. Dora Tang, T.-Y., Hak, C. R. C., Thompson, A. J., Kuimova, M. K., Williams, D. S., Perriman, A. W. & Mann, S. Fatty acid membrane assembly on coacervate microdroplets as a step towards a hybrid protocell model. *Nat. Chem.* **6,** 527–533 (2014).

16. Thiele, J., Ma, Y., Foschepoth, D., Hansen, M. M. K., Steffen, C., Heus, H. A. & Huck, W. T. S. DNA-functionalized hydrogels for confined membrane-free in vitro

transcription/translation. *Lab Chip* **14,** 2651–2656 (2014).

17. Aufinger, L. & Simmel, F. C. Artificial Gel-Based Organelles for Spatial Organization of Cell-Free Gene Expression Reactions. *Angew. Chem. Int. Ed.* **57,** 17245–17248 (2018).

18. Niederholtmeyer, H., Chaggan, C. & Devaraj, N. K. Communication and quorum sensing in non-living mimics of eukaryotic cells. *Nat. Commun.* **9,** 1–8 (2018).

19. Huang, X., Li, M., Green, D. C., Williams, D. S., Patil, A. J. & Mann, S. Interfacial assembly of protein-polymer nano-conjugates into stimulus-responsive biomimetic protocells. *Nat. Commun.* **4,** 2239 (2013).

20. Frey, R., Mantri, S., Rocca, M. & Hilvert, D. Bottom-up Construction of a Primordial Carboxysome Mimic. *J. Am. Chem. Soc.* **138,** 10072–10075 (2016).

21. Peters, R. J. R. W., Marguet, M., Marais, S., Fraaije, M. W., van Hest, J. C. M., & Lecommandoux, S. Cascade reactions in multicompartmentalized polymersomes. *Angew. Chem. Int. Ed.* **53,** 146–150 (2014).

22. Rodríguez-Arco, L., Li, M. & Mann, S. Phagocytosis-inspired behaviour in synthetic protocell communities of compartmentalized colloidal objects. *Nat. Mater.* **16,** 857–863 (2017).

23. Milo, R., Phillips, R. & Orme, N. *Cell Biology by the Numbers* (Garland Science, New York, 2015).

24. Porte, G. Lamellar phases and disordered phases of fluid bilayer membranes. *J. Phys. Condens. Matter* **4,** 8649–8670 (1992).

25. Menger, F. M. & Sykes, B. M. Anatomy of a Coacervate. *Langmuir* **14,** 4131–4137 (1998).

26. Conn, C. E. & Drummond, C. J. Nanostructured bicontinuous cubic lipid self-assembly materials as matrices for protein encapsulation. *Soft Matter* **9,** 3449–3464 (2013).

27. Strey, R., Schomacker, R., Roux, D., Nallet, F. & Olsson, U. Dilute lamellar and L_3 phases in the binary water-C12E5 system. *J. Chem. Soc. Faraday Trans.* **86,** 2253–2261 (1990).

28. Strey, R., Jahn, W., Porte, G. & Bassereau, P. Freeze fracture electron microscopy of dilute lamellar and anomalous isotropic (L_3) phases. *Langmuir* **6,** 1635–1639 (1990).

29. Peresypkin, A. V. & Menger, F. M. Zwitterionic Geminis. Coacervate Formation from a Single Organic Compound. *Org. Lett.* **1,** 1347–1350 (1999).

30. Imura, T., Yanagishita, H. & Kitamoto, D. Coacervate formation from natural glycolipid: One acetyl group on the headgroup triggers coacervate-to-vesicle transition. *J. Am. Chem. Soc.* **126,** 10804–10805 (2004).

31. Angelov, B., Angelova, A., Mutafchieva, R., Lesieur, S., Vainio, U., Garamus, V., Jensen, G. V. & Pedersen, J. S. SAXS investigation of a cubic to a sponge (L_3) phase transition in self-assembled lipid nanocarriers. *Phys. Chem. Chem. Phys.* **13**, 3073–3081 (2011).

32. Brea, R. J., Bhattacharya, A., Bhattacharya, R., Song, J., Sinha, S. K. & Devaraj, N. K Highly Stable Artificial Cells from Galactopyranose-Derived Single-Chain Amphiphiles. *J. Am. Chem. Soc.* **140,** 17356-17360 (2018).

33. Bhattacharya, A., Brea, R. J., Song, J., Bhattacharya, R., Sinha, S. K. & Devaraj, N. K. Single-Chain β-D-Glycopyranosylamides of Unsaturated Fatty Acids: Self-Assembly

Properties and Applications to Artificial Cell Development. *J. Phys. Chem. B* **123,** 3711–3720 (2019).

34. Maldonado, A., Urbach, W., Ober, R. & Langevin, D. Swelling behavior and local topology of an L_3 (sponge) phase . *Phys. Rev. E* **54,** 1774–1778 (1996).

35. Pabst, G., Rappolt, M., Amenitsch, H. & Laggner, P. Structural information from multilamellar liposomes at full hydration: Full q-range fitting with high quality X-ray data. *Phys. Rev. E* **62,** 4000–4009 (2000).

36. Valldeperas, M., Dabkowska, A. P., Pálsson, G. K., Rogers, S., Mahmoudi, N., Carnerup, A., Barauskas, J. & Nylander, T. Interfacial properties of lipid sponge-like nanoparticles and the role of stabilizer on particle structure and surface interactions. *Soft Matter* **15,** 2178–2189 (2019).

37. Garenne, D., Beven, L., Navailles, L., Nallet, F., Dufourc, E. J. & Douliez, J-P. Sequestration of Proteins by Fatty Acid Coacervates for Their Encapsulation within Vesicles. *Angew. Chem. Int. Ed.* **55,** 13475–13479 (2016).

38. Winzer, K., Falconer, C., Garber, N. C., Diggle, S. P., Camara, M. & Williams, P. The *Pseudomonas aeruginosa* lectins PA-IL and PA-IIL Are Controlled by Quorum Sensing and by RpoS. *J. Bacteriol.* **182,** 6401–6411 (2000).

39. Johannes, L., Jacob, R. & Leffler, H. Galectins at a glance. *J. Cell Sci.* **131,** jcs208884 (2018).

40. Daber, R., Stayrook, S., Rosenberg, A. & Lewis, M. Structural Analysis of Lac Repressor Bound to Allosteric Effectors. *J. Mol. Biol.* **370,** 609–619 (2007).

41. Shimizu, Y., Inoue, A., Tomari, A., Suzuki, T., Yokogawa, T., Nishikawa, K. & Ueda, T. Cell-free translation reconstituted with purified components. *Nat. Biotechnol.* **19,** 751–755 (2001).

42. Dahms, N. M., Olson, L. J. & Kim, J. J. P. Strategies for carbohydrate recognition by the mannose 6-phosphate receptors. *Glycobiology* **18,** 664–678 (2008).

43. Schwarz, D. S. & Blower, M. D. The endoplasmic reticulum: Structure, function and response to cellular signaling. *Cell. Mol. Life Sci.* **73,** 79–94 (2016).

44. Avalos, J. L., Fink, G. R. & Stephanopoulos, G. Compartmentalization of metabolic pathways in yeast mitochondria improves the production of branched-chain alcohols. *Nat. Biotechnol.* **31,** 335–341 (2013).

45. Zhou, Y. J., Buijs, N. A., Zhu, Z., Gómez, D. O., Boonsombuti, A., Siewers, V., & Nielsen, J. Harnessing Yeast Peroxisomes for Biosynthesis of Fatty-Acid-Derived Biofuels and Chemicals with Relieved Side-Pathway Competition. *J. Am. Chem. Soc.* **138,** 15368–15377 (2016).

46. Itzhak, D. N., Tyanova, S., Cox, J. & Borner, G. H. H. Global, quantitative and dynamic mapping of protein subcellular localization. *Elife* **5,** e16950 (2016).

47. Shin, Y., Berry, J., Pannucci, N., Haataja, M. P., Toettcher, J. E., & Brangwynne, C. P. Spatiotemporal Control of Intracellular Phase Transitions Using Light-Activated optoDroplets. *Cell* **168,** 159–171 (2017).

48. Beyer, H. M., Thomas, O. S., Riegel, N., Zurbriggen, M. D., Weber, W. & Hörner, M.

Generic and reversible opto-trapping of biomolecules. *Acta Biomater.* **79,** 276–282 (2018).

49. Audas, T. E., Jacob, M. D. & Lee, S. The nucleolar detention pathway: A cellular strategy for regulating molecular networks. *Cell Cycle* **11,** 2059–2062 (2012).

50. Shi, X., Wu, T., Cole, C. M., Devaraj, N. K. & Joseph, S. Optimization of ClpXP activity and protein synthesis in an E. coli extract-based cell-free expression system. *Sci. Rep.* **8,** 3488 (2018).

51. Gatsogiannis, C., Balogh, D., Merino, F., Sieber, S. A. & Raunser, S. Cryo-EM structure of the ClpXP protein degradation machinery. *Nat. Struct. Mol. Biol.* **26,** 946–954 (2019).

52. Kang, M., Andreani, M. & Kenworthy, A. K. Validation of normalizations, scaling, and photofading corrections for FRAP data analysis. *PLoS One* **10,** 1–28 (2015).

53. Bhattacharya, A., Brea, R. J., Niederholtmeyer, H. & Devaraj, N. K. A minimal biochemical route towards de novo formation of synthetic phospholipid membranes. *Nat. Commun.* **10**, 300, (2019).

54. Stenger, F. & Voigt, A. Interactive Evolution of a Bicontinuous Structure. Leonardo. **1**, 1-7 (2018).